Available online at https://link.springer.com/journal/42241
http://www.jhydrodynamics.com
Journal of Hydrodynamics, 2022, 34(4): 681-699
https://doi.org/10.1007/s42241-022-0057-9

Numerical investigation of the dynamics of flexible vegetations in turbulent open-channel flows

Dong Xu, Jia-ning Liu, Yun-feng Wu, Chun-ning Ji*
State Key Laboratory of Hydraulic Engineering Simulation and Safety, Tianjin University, Tianjin 300072, China

(Received April 13, 2022, Revised June 11, 2022, Accepted July 3, 2022, Published online September 2, 2022)

Abstract: Aquatic vegetations widely exist in natural rivers and play an essential role in the evolution of the water environment and ecosystem by changing the river's hydrodynamic characteristics and transporting sediments and nutrition. In reality, most aquatic vegetations are highly flexible, which invalidates the "rigid-cylinder" assumption widely adopted in many literatures. To explore the dynamics of submerged flexible vegetation in open-channel flows and its feedback to turbulent flow structures, numerical simulations are carried out using an in-house fluid-structure interaction (FSI) solver. In the simulations, the geometry of vegetation plants is grid-resolved, the turbulent flow is simulated using the large eddy simulation (LES), the dynamics of the flexible plants are solved using the vector form intrinsic finite element (VFIFE) method, and the turbulent flow and the plants are two-way coupled using the immersed boundary (IB) method. The dynamic responses of the flexible vegetation with different plant flexibility, spacing, and submergence are investigated. Simulation results show that flexible plants are subjected to complex flow-induced vibrations (FIVs) rather than static bending. The FIV involves both streamwise and cross-flow motions driven by the small-scale vortex shedding around the plants and the large-scale Kelvin-Helmholtz (K-H) vortices developed in the vegetation canopy layer. The vegetations exhibit pulsive wave motion of different patterns in relatively long and narrow open channels. Compared with the open-channel flows with static plants with equivalent bending deformation, the dynamic responses of flexible plants may increase the turbulent Reynolds stress of the open-channel flow by 70%-100% and increase the invasion depth of the K-H vortices by 30%-50%.

Key words: Flexible vegetation, dynamic responses, flow-induced vibration (FIV), fluid-structure interaction (FSI)

Introduction

As widely existing in natural rivers, aquatic vegetation significantly impacts energy transport and the material cycle in the estuarine ecosystem[1-2]. The influence of submerged or emergent vegetations on open channel flows is extremely complex. By simplifying the vegetation plants as rigid cylinders, several theories for the vegetated flow have been developed, e.g., the vertical flow velocity profile partition and the wake vortex shedding model behind cylinders, etc.[3-6]. Such theories significantly add to our knowledge on the flow resistance in vegetated channels on both micro and macro scales etc.

However, rigid vegetations are scarce in nature. The vast majority of vegetations are flexible, e.g., Young's modulus of a kind of kelp is 1.2×10^7 N·m^{-2}[7], and that of seagrass can even reach 2.4×10^9 N·m^{-2}[8-9]. The motion of submerged vegetations significantly changes the flow structures in open-channel flows, thus influencing the sediment movement and water body exchanges. Therefore, flexible plant models with real flexibility can better reflect the dynamic characteristics of the vegetations. Only quite limited studies have focused on the influence of plants' flexibility on the flows[10-12]. Recent research implies that the flexibility of plants significantly affects the flow profiles and the invasion depth of Kelvin-Helmholtz (K-H) vortexes into vegetation patches. The maximum turbulence energy occurs near the crest and trough of the bed and around the top of the vegetation patch, where the relative flow velocity is large. Further confirming these conclusions, Huai et al.[13] found that the dominant dimensionless frequency was surprisingly invariant at around 0.027 despite large differences in vegetation densities for the preset water depth. On the other hand, the impact of the flow on the vegetation dynamics has also been noticed. Luhar and Nepf[11] predicted the deformation of flexible plants based on the balance of forces, including the flow inertia force, the gravitational force, and the restoring force due to vegetation deformation and

Project supported by the National Natural Science Foundation of China (Grant Nos. 5217090155, 51979186 and 51779175).
Biography: Dong Xu (1980-), Male, Ph. D.,
Associate Professor, E-mail: xudong@tju.edu.cn
Corresponding author: Chun-ning Ji,
E-mail: cnji@tju.edu.cn

buoyancy. The deformation of the flaky and flexible vegetation subjected to outer flow is mainly affected by the Cauchy number and the ratio of gravitational force to the restoring force. Silva-Leon and Cioncolini[14] found that the deflection angle of vegetation plants decreases with the increasing Reynolds number, following a sigmoidal trend. Besides, many other studies[14-17] investigated the motions of two-dimensional flexible vegetations or 3-D flaky flexible vegetations with a different configuration of plants. It was widely found that the motion of plants is highly influenced by the Reynolds number based on a characteristic length of the plant height, the non-dimensional bending stiffness, and the mass ratio. Various modes of dynamics are reported for a single plant, including the static, flapping, chaos, and lodging modes. These modes are also observed in the dynamic responses of two- and multiple-plant dynamic systems. In addition, the two-plant system also demonstrates a cavity oscillation mode when the non-dimensional bending stiffness is high while the multiple-plant system further shows complex waving modes including the Monami phenomenon.

Despite the valuable insight gained in these studies, understanding the dynamics of flexible vegetations in turbulent open-channel flows is still far from complete. These studies either focused on the turbulent flow over and through rigid vegetations or investigated the dynamic motions of a small number of vegetation plants, making it hard to analyze the vegetated flow or the large-scale vegetation waves. A big challenge lies in the fact that to accurately simulate the complex interaction of turbulent flow and flexible vegetation plants requires extremely fine grids resolving the plant's geometry. Such numerical simulations are very time-consuming, and we are not aware of any simulations of these kinds have been performed. In this study, a series of numerical simulations are carried out to explore the dynamics of submerged flexible vegetations in the open-channel flow and their feedback on turbulent flow. Based on the simulation results, the effects of the plant flexibility, spacing, and submergence on dynamic responses of the flexible vegetation are investigated.

1. Methodology

1.1 *Fluid-structure interaction (FSI) solver*

With the great advances in computer technology, large eddy simulation (LES) has been widely applied to the numerical simulations of the flow around bluff bodies and advancing the understanding of flow structures and three-dimensional coherent structures[18-21]. The application of LES in the open-channel flow past submerged circular plants gradually plays an increasingly important role[22-24].

In LES, the fluid motion is filtered into two parts, which are resolved by the transient, spatially filtered continuity equation and Navier-Stokes equations, and the sub-grid scale model, respectively. The spatially filtered governing equations for incompressible fluid flow are:

$$\frac{\partial \overline{u}_i}{\partial t}+\frac{\partial}{\partial x_j}(\overline{u}_i\overline{u}_j)=-\frac{1}{\rho}\frac{\partial \overline{p}}{\partial x_i}+\nu\frac{\partial^2 \overline{u}_i}{\partial x_j^2}+\frac{1}{\rho}\frac{\partial \tau_{ij}}{\partial x_j}+f_i,$$

$$\frac{\partial \overline{u}_i}{\partial x_i}=0 \tag{1}$$

where u_i is the velocity component (i, j are the tensor indicators), t is the time, x_i represents the three directions of the Cartesian coordinate system (x, y and z), p is the pressure, ρ is the fluid density, f_i denotes the body force including the force due to the immersed boundary, v is the kinematic viscosity includes the molecular and eddy viscosities and τ_{ij} is the sub-grid stress tensor, representing the influence of the filtered small-scale turbulent structure on the large-scale. The sub-grid model used in this paper is the Smagorinsky eddy viscosity model[25]

$$\tau_{ij}^{\text{smag}}=2\rho(C_S\Delta)^2\left|\overline{S}\right|\overline{S}_{ij}+\frac{1}{3}\tau_{kk}\delta_{ij} \tag{2}$$

where C_S is the Smagorinsky constant ($C_S=0.1$ for the current study), Δ is the filtering scale selected for LES, the magnitude of the strain rate $\left|\overline{S}\right|=(2\overline{S}_{ij}\overline{S}_{ij})^{1/2}$, $\overline{S}_{ij}$ is the rate of strain tensor for the resolved scale and δ_{ij} is the Kronecker delta.

The finite volume method is used for spatial discretization, while the second-order Adam-Bashforth scheme is applied for time marching.

Vegetation plants are modeled as flexible cylinders, and the dynamic responses of these plants are simulated by using the vector form intrinsic finite element (VFIFE) method. Based on the point value description and the vector theory, the VFIFE method has apparent advantages in simulating flexible structures' nonlinear or discontinuous dynamic behaviors. According to the point value description method, the structure is discretized into a certain number of nodes. The motion of each node satisfies Newton's second law, and the differential equations of translation and rotation of the node are:

$$m\ddot{x}+\alpha m\dot{x}=F,\quad I\ddot{\theta}+\alpha I\dot{\theta}=M \tag{3}$$

where m and I are the mass and inertia moment matrix of the node, respectively, $\dot{x}$, $\ddot{x}$ and $\dot{\theta}$, $\ddot{\theta}$ are the velocity, acceleration, angular velocity, and angular acceleration of the node, respectively, α is the structural damping coefficient, while F and M are the resultant force and moment. The force F is the sum of the external hydrodynamic force and the internal forces from the solid elements. An explicit iterative-based central differential scheme is used to solve the governing equations. More details of the VFIFE are referred to in the works of Shih et al.[26], Ting et al.[27-28].

The immersed boundary (IB) method is introduced to couple the fluid flow and structural deformation by adding an extra body force to the momentum equation. A Cartesian grid is used for the flow solver, and the structure is represented by a series of IB points. The extra body force is calculated by satisfying the fluid-structure boundary conditions on the IB points. Interpolation and extrapolation functions are applied to exchange velocity and force between the fluid grid and the IB points. The IB method avoids the complex body-fitted grid and can easily deal with the FSI problems with moving/deforming structures[29]. Readers are referred to our previous works of Ji et al.[30], Chen et al.[31-32] for further details on the IB method.

In this study, the vegetation plant is simplified as a slender cantilever rod which is further discretized into a series of 3-D beam elements following the axis of the plant. Then, IB points are generated based on the coordinates and azimuthal angles of the elements and the rod diameter to reconstruct the plant's surface, as shown in Fig. 1.

1.2 *Validation cases*

Two cases are adopted to validate the numerical model. The first case is the deformation of a cantilever plate under different uniformly distributed loads. The deflection of the plate is compared with the theoretical solution to investigate the effect of spatial discretization. The parameters of the plate and the settings of the validation case are shown in Table 1.

Table 1 Parameters of the plate and settings of the validation case of a cantilever plate

Parameter	Value
Length, l /m	0.050
Width, b /m	0.010
Height, h /m	0.002
Density, ρ /(kg·m^{-3})	678
Elastic modulus, E /Pa	5×10^{5}
Poisson's ratio, μ	0.4
Distributed load, q /(N·m^{-1})	1×10^{-2}, 2×10^{-2}, 4×10^{-2}, 8×10^{-2},
Number of solid elements, n_s	10, 25, 50

Figure 2 shows the relative error of the deflection at the free end of the cantilever beam against grid resolution with different distributed loads. It proves the high accuracy of the adopted numerical methodology of the solid solver when the plate is discretized with more than 25 elements.

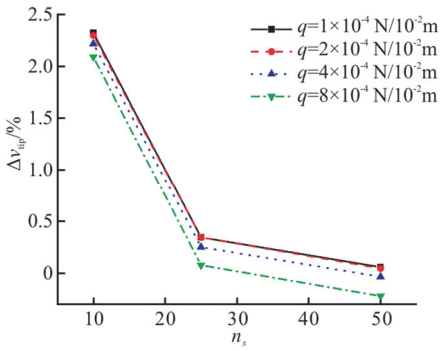

Fig. 2 (Color online) The relative error of the deflection at the free end of the cantilever beam against grid resolution with different distributed loads

To further verify the accuracy of the FSI model, the deformation and fluid forces on the cantilever plate in the open-channel flow are simulated following the experiment of Luhar and Nepf[11]. The computational setup and boundary conditions are shown in Fig.

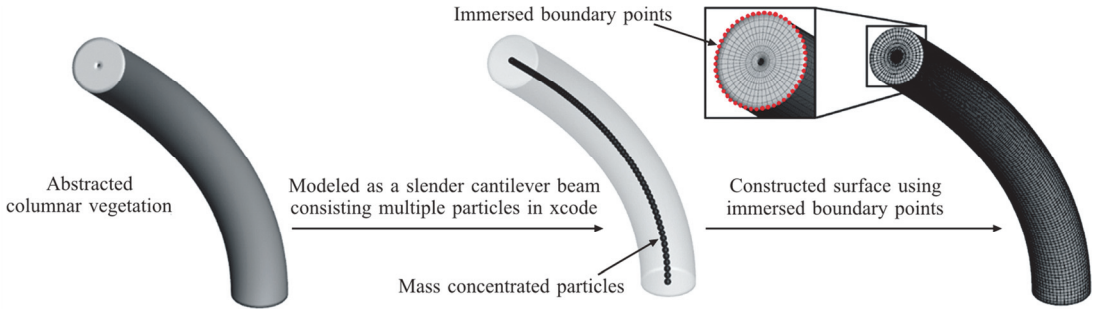

Fig. 1 (Color online) Schematic of the flexible plant model

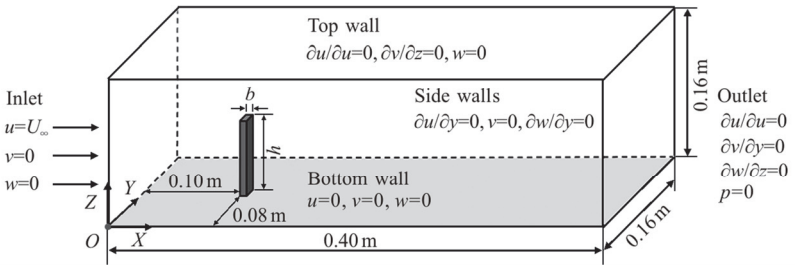

Fig. 3 Schematic of the computational domain and boundary conditions of a cantilever plate in the open-channel flow

Table 2 Parameters of the plate and settings of validation cases

Case	Number of grids, $n_x \times n_y \times n_z$	Aspect ratio, b/h	Number of elements, n_s	Inflow velocity, U_∞ /(m·s^{-1})
1	128×48×64	5	25	0.160
2	256×96×128	10	80	0.160
3	384×160×192	16	80	0.160
4	512×192×256	20	100	0.160
5	384×160×192	16	80	0.036
6	384×160×192	16	80	0.110
7	384×160×192	16	80	0.160
8	384×160×192	16	80	0.270

3. The parameters as listed in Table 2 are the same as those adopted in the experiments of Luhar and Nepf[11].

As shown in Fig. 4, when the number of grids is higher than 384×160×192 and the element number is larger than $n_s = 80$, the relative errors δ of w_x/b, F_x are less than 1%, which proves that the numerical results are grid-independent. Here, w_x is the deflections of the plate at the free end in the x directions, and F_x is the flow resistance of the plant. As shown in Fig. 5, the simulated results of F_x show good agreement with the experimental data, signifying the high accuracy of the FSI model.

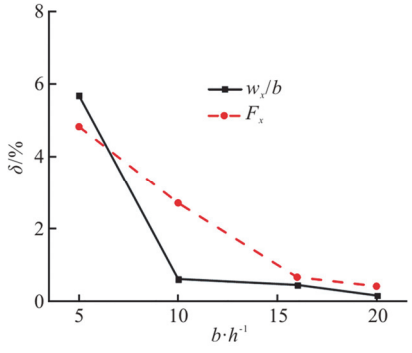

Fig. 4 (Color online) The relative error of the deflection and flow resistance against grid resolution

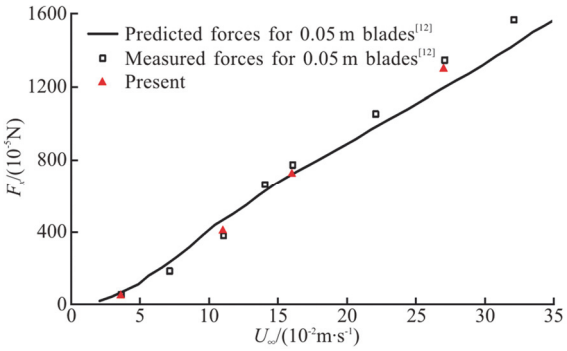

Fig. 5 (Color online) Verification of the simulated fluid force on the flexible vegetation against experiment data

2. Simulation cases

2.1 *Computational domain and grid*

The computational domain and plant arrangement are shown in Fig. 6. The length (L), the width (W) of the computational domain are $384d$, $16d$, respectively, with d being the diameter of the cylindrical plant. Three values of the computational domain height (H) are adopted to change the vegetation submergence ratio. Up to 720 vegetation plants, with a height of $10d$, are mounted on the bed in a staggered arrangement. The spacing of the plants is $D_x = 4d - 8d$ in the streamwise direction, $D_y = 2d - 4d$ in the transverse direction. The periodic con-

dition is implemented at the inflow and outflow boundaries, with the non-slip rough-wall boundary condition imposed on the bottom wall. The free-slip boundary condition is prescribed on the two sides and the top. By adding a streamwise body force, an equivalent bed slope of $S = 4\times10^{-4}$ is introduced into the open channel, which drives the fluid flow. A uniform mesh is adopted to discretize the computational domain, and the grid size in three directions is $\Delta = d/8$. The computational grid amount ranges from 37 748 736 to 62 914 560 for various cases.

2.2 *Simulation parameters*

According to the physical parameters of aquatic vegetations measured by Luhar and Nepf[11], the diameter of the cylinder is set as $d = 0.005$ m, the cylinder's height is $l = 0.050$ m and its density is $\rho = 3\times10^3$ kg / m^3. In the simulations, four different stiffness ratios (denoted K1-4), four different porosities (A1-4), and three different submergences (H1-3) are considered. To compare with the flexible cases, eight cases of rigid vegetations (R1-7, Rd) are simulated with different bending postures, corresponding to different equivalent stiffness ratios. Simu-

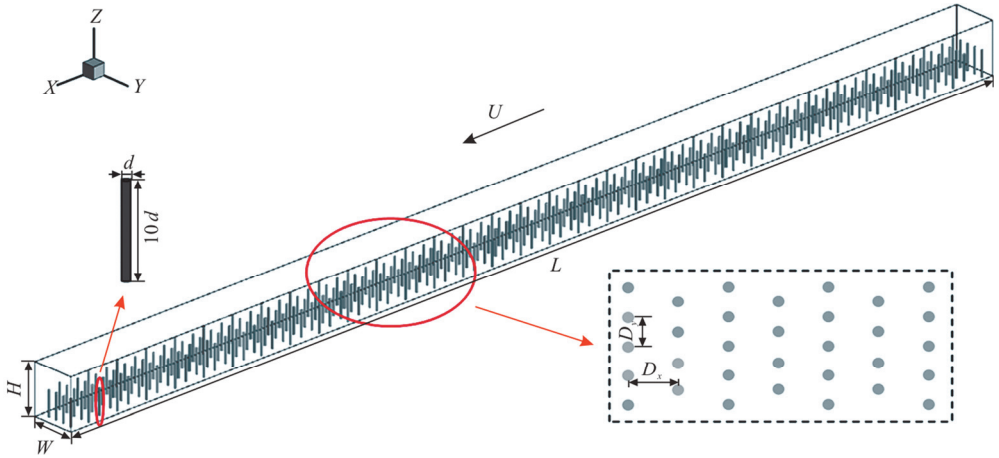

Fig. 6 (Color online) Schematic of the computational domain and vegetation configuration

Table 3 Simulation parameters for vegetations with different characteristic properties

Cases	Size, $L\times W\times H$	Planting spacing, $D_L\times D_W$	Number of plants, N	Bending stiffness, EI /10^{-8}N·m^2	Spacing, $a=\frac{ldN}{LW}$	Submergence, $\eta=\frac{H}{l}$	Stiffness ratio, $K=\frac{1}{Ca}=\frac{2EI}{\rho_f C_D d l^3 U_{\mathrm{ref}}^2}$
A2H1K1	$384d\times16d\times20d$	$6d\times3d$	288	4.90	0.469	2.0	0.044
A2H1K2	$384d\times16d\times20d$	$6d\times3d$	288	9.60	0.469	2.0	0.087
A2H1K3	$384d\times16d\times20d$	$6d\times3d$	288	19.6	0.469	2.0	0.174
A2H1K4	$384d\times16d\times20d$	$6d\times3d$	288	39.2	0.469	2.0	0.347
A1H1K2	$384d\times16d\times20d$	$8d\times4d$	168	9.60	0.273	2.0	0.087
A3H1K2	$384d\times16d\times20d$	$4d\times4d$	336	9.60	0.547	2.0	0.087
A4H1K2	$384d\times16d\times20d$	$4d\times2d$	720	9.60	1.172	2.0	0.087
A2H2K2	$384d\times16d\times16d$	$6d\times3d$	288	9.60	0.469	1.6	0.087
A2H3K2	$384d\times16d\times12d$	$6d\times3d$	288	9.60	0.469	1.2	0.087
A2H1R1	$384d\times16d\times20d$	$6d\times3d$	288	-	0.469	2.0	0.001
A2H1R2	$384d\times16d\times20d$	$6d\times3d$	288	-	0.469	2.0	0.003
A2H1R3	$384d\times16d\times20d$	$6d\times3d$	288	-	0.469	2.0	0.010
A2H1R4	$384d\times16d\times20d$	$6d\times3d$	288	-	0.469	2.0	0.044
A2H1R5	$384d\times16d\times20d$	$6d\times3d$	288	-	0.469	2.0	0.087
A2H1R6	$384d\times16d\times20d$	$6d\times3d$	288	-	0.469	2.0	0.174
A2H1R7	$384d\times16d\times20d$	$6d\times3d$	288	-	0.469	2.0	0.347
A2H1Rd	$384d\times16d\times20d$	$6d\times3d$	288	-	0.469	2.0	-

lation parameters are listed in Table 3.

3. Results

For convenience, the instantaneous value, the time-averaged value, and the space-/plant-averaged value of a variable x are denoted as x, $\bar{x}$, $\langle x \rangle$, respectively. Following Etminan et al.[33], two reference flow velocities are defined in this paper. One is the pore velocity U_{pore}, which is related to the time- and plant-averaged projection height $\langle \bar{h}_v \rangle$ and the spacing of vegetation, the other is the bulk velocity U_{bulk}, which is the time- and space-averaged flow velocity in the computational domain.

(1) The pore velocity

$$U_{\text{pore}} = \frac{\int_0^{\langle \bar{h}_v \rangle} \langle \bar{u}(z) \rangle \mathrm{d}z / \bar{h}_v}{1 - (N\pi \mathrm{d}^2 / 4LW)} \tag{4}$$

(2) The bulk velocity

$$U_{\text{bulk}} = \int_0^H \frac{\langle \bar{u}(z) \rangle \mathrm{d}z}{H} \tag{5}$$

where N is the number of vegetations, L, W and H are the channel's length, width and height, d is the vegetation diameter and $u(z)$ is the streamwise flow velocity at a height of z.

3.1 *Vegetation deformation under the force action of fluids*

Figure 7 shows the time history of the plant-averaged non-dimensional projection height h_v / l of the vegetation plants at different values of the stiffness ratio K. The projection height ranges from 0.62 for highly flexible vegetations, to 0.98 for relatively stiff cases. The larger the value of K, the larger the value of h_v / l, signifying that the vegetation deforms less. Besides, the cases with larger stiffness ratios approach their quasi-steady-state much faster than the highly flexible ones. For all cases, the vegetations reach a fully deformed state statistically within a non-dimensional time around 150. The fluctuation of projection height in highly flexible cases, A2H1K1, A2H1K2, implies low-frequency oscillations and retarded responses of vegetations after an immediate action of fluid force at the beginning stage of the simulation.

In all simulation cases, plants with relatively large numbers, ranging from 168 to 720, are mounted onto the bed in staggered arrangements. The periodic boundary adopted in the streamwise direction further expands the scope of the computational domain. Under such conditions, the interior of the vegetation can be regarded as a relatively uniform porous medium, and the plants may bend in different directions with different amplitudes dynamically. Taking a snapshot of the simulated results, the average deformation of plants in the streamwise/transverse direction $\langle \bar{D}_x \rangle / |\langle \bar{D}_y \rangle|$ and the time- and plant-averaged projection height $\langle \bar{h}_v \rangle$ can be worked out, see Table 4. The streamwise deformation of the plants ranges from $0.181l$ to $0.704l$, which is around 16-35 times larger than the spanwise(cross-flow) direction, namely $0.011l$ to $0.024l$. Unlike the cross-flow component, the streamwise deformation is significantly influenced by the plants' stiffness ratio and the spacing between adjacent plants. When the spacing decreases from cases A1H1K2 to A4H1K2, namely the area-averaged distribution density of plants increases by up to 4 times, and the plants' streamwise deformation decreases by 29%, 51%, respectively. Flow submergence depth has little influence on the plants' deformation, see cases A2H1K2, A2H2K2 and A2H3K2. Compared with the streamwise deformation, the cross-flow deformation is much less sensitive to stiffness ratio, plant spacing, and submergence depth.

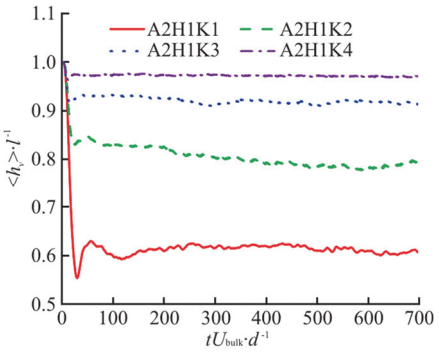

Fig. 7 (Color online) Time histories of the plant-averaged non-dimensional projection height at different stiffness ratios

Table 4 The average deformation of plants in the streamwise/transverse direction

Case	$\langle \bar{D}_x \rangle$	$\lvert\langle \bar{D}_y \rangle\rvert$	$\langle \bar{D}_x \rangle / \lvert\langle \bar{D}_y \rangle\rvert$
A2H1K1	0.704	0.020	34.93
A2H1K2	0.530	0.022	24.66
A2H1K3	0.321	0.018	17.74
A2H1K4	0.181	0.011	16.14
A1H1K2	0.646	0.018	36.55
A3H1K2	0.458	0.024	19.25
A4H1K2	0.317	0.022	14.45
A2H2K2	0.306	0.014	21.21
A2H3K2	0.361	0.018	20.09

Under the force action of the fluid, all of the vegetations are subjected to periodic oscillations with complex modes. At an instanuous moment, the bending state of one particular plant may be at any random phase of the oscillation. Statistics of all of the plants may smooth out such randomness. Therefore, statistical analysis using the probability density curves (PDC) is carried out for a snapshot of all of the plants at a moment when the flows fully develop, see Figs. 8-10. For all of these figures, the variable N on the vertical axis refers to the number of plants within a specific range of deformations.

The streamwise deformations, $\overline{D}_x$, demonstrate two-peak histogram distributions, see Fig. 8, which are quite different from the centrosymmetric normal distribution corresponding to uniform random numbers. This implies that the spatial distribution of the plants' deformations is not uniformly random. The plants tend to be either highly deformed or weakly deformed, with a much lower probability for the transition status in between exhibiting medium deformations. The first peak on the left is linked with relatively smaller deformations of plants compared with the second peak on the right side of the curve. The height of the first peak almost doubles that of the second peak. This means that more plants exhibit relatively lower deformations, rather than highly deformed status corresponding to the second peak of the PDC curve. Such probability distribution also implies that if the middle value is taken between the lowest and the highest deformation, the estimation for plants' deformation could be incorrect during flow-vegetation interaction analysis. This is especially true for highly flexible vegetations, see Figs. 8(a)-8(c), when compares with the relatively rigid vegetations, see Fig. 8(d).

The cross-flow deformations in the spanwise direction, $\overline{D}_y$, demonstrate three-peak histogram distributions, see Fig. 9. The distributions are centrosymmetric in general, but also different from the normal distributions. The highest peak of the PDC sites in the middle, with two lower peaks on both sides symmetrically. This implies that most plants are at the medium status without obvious spanwise deformations. There are two relatively lower peaks symmetrically distributed on both sides of the PDC, which implies an equivalent chance for the plants to swing to the left and the right side of the channel. With the increase of stiffness ratio K, the range of plant deformation decreases, and the secondary peaks gradually approach the main. However, the distribution law of $\overline{D}_x$, $\overline{D}_y$ and $\overline{h}_v$ does not change with stiffness ratio, and the streamwise deformation is always stronger than that of the transverse direction. The spanwise swing of the plants may lead to increases in the obstacle area projected in the flow directions and hence rises in flow resistances.

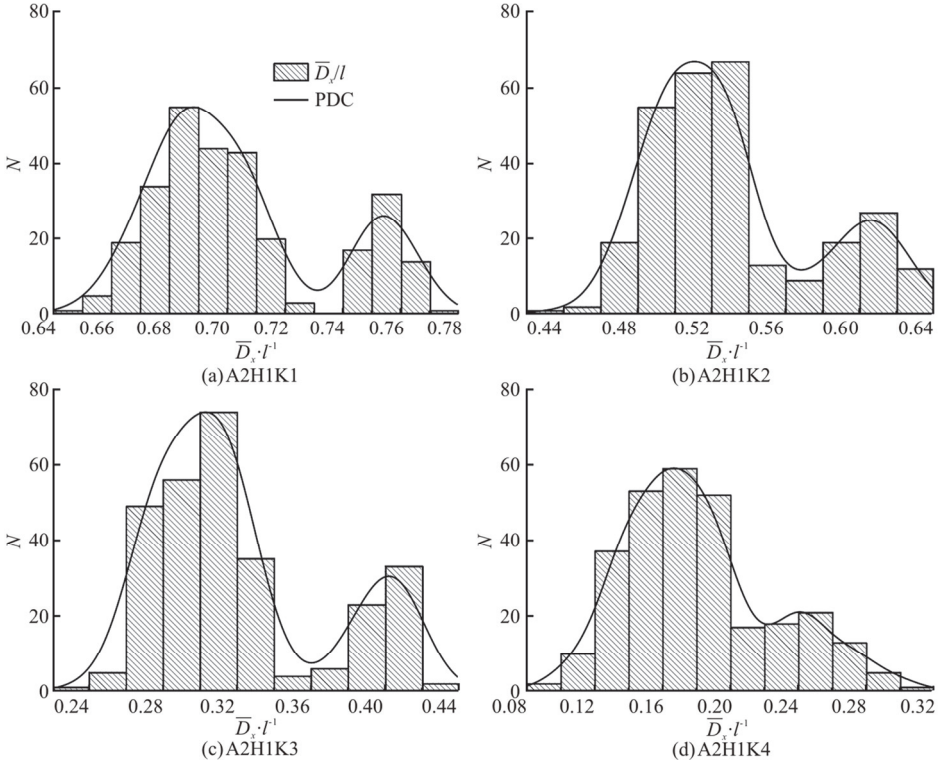

Fig. 8 Histogram of the probability distribution for streamwise deformation of plants with various stiffness ratios

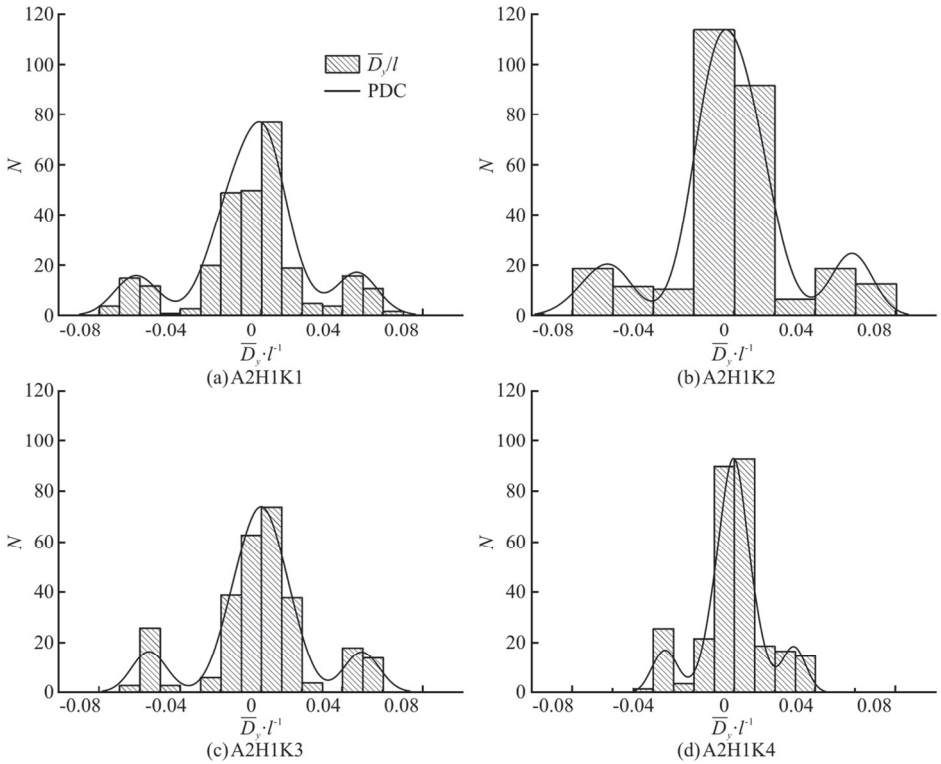

Fig. 9 Histogram of the probability distribution for cross-flow deformation of plants with various stiffness ratios

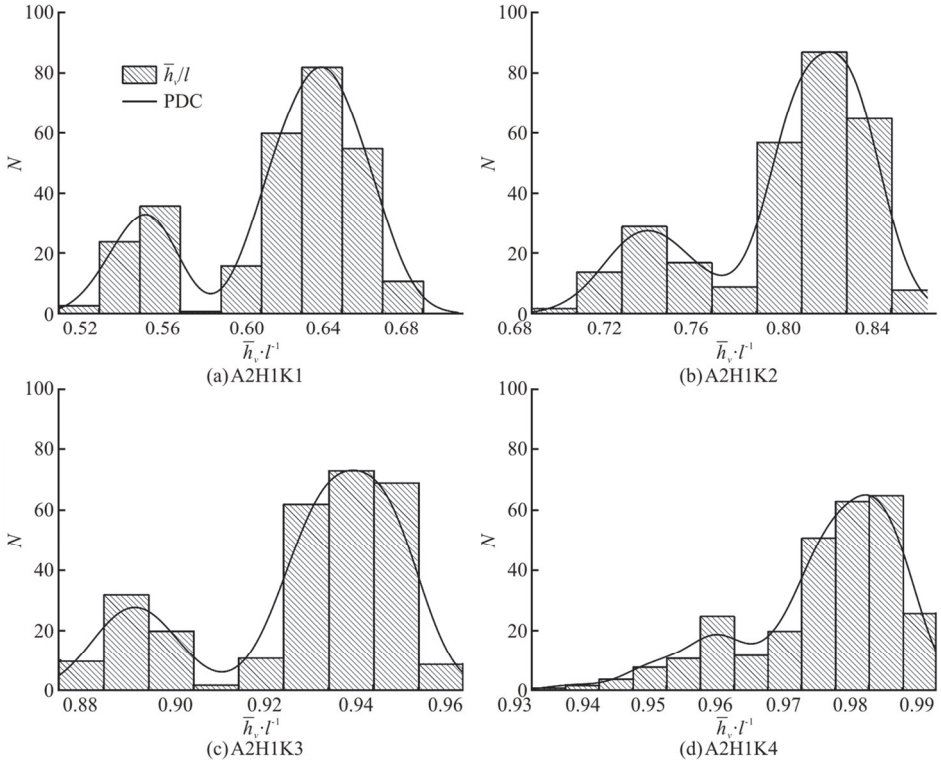

Fig. 10 Histogram of the probability distribution for projection height of plants with various stiffness ratios

The projection height of the plants, $\overline{h}_v$, exhibits two-peak histogram distributions, see Fig. 10. Unlike the PDC for the streamwise deformation, see Fig. 8, the highest peaks site on the right side of the curve. This tendency is consistent with the deformation distribution described by the streamwise direction consi-

dering that the projection height is mainly caused by the streamwise deflection. Larger deflections reflect smaller projection height of the vegetations. Therefore, the PDC for the projection height exhibits antisymmetric distributions compared with the streamwise deformation.

To investigate the influence of distribution density of vegetations on their deformation, simulations with 4 different plant arrangements are carried out. The spacing between plants is $8d \times 4d$, $6d \times 3d$, $4d \times 4d$ and $4d \times 2d$, respectively. The occupied areas per plant are $32d^2$, $18d^2$, $16d^2$ and $8d^2$, respectively. Taking the first case as a base, the vegetation density increases to 177.8%, 200% and 400% of the original in the following cases. See Figs. 11, 12 for the influences of vegetation spacing on the cross-flow deformation and the projection height on the PDC curve. It can be seen that with the increase of the vegetation density, from case A1H1K2 to case A4H1K2, the plants' deformation reduces at a magnitude of around 50%, which can also be seen in Table 4. This implies that the jamming of the vegetations restrains their oscillations when the spacing is relatively small. When the vegetation density increases, the secondary peak on the PDC curve gradually moves towards the main peak, and the original broadly distributed probability density, see Figs.11(a), 12(a), gradually concentrates to a relatively narrow band, see Figs. 11(d), 12(d). This can be interpreted by the overcrowding of vegetation leads to strong interference among plants and finally suppress their free vibrations under the flow actions.

To investigate the influence of submergence depth of vegetations on their deformation, simulations with 3 different plant arrangements are carried out. The water depth compared with vegetation height is 2.0, 1.6 and 1.2, respectively. See Figs. 13, 14 for the influences of submergence depth on the cross-flow deformation and the projection height on the PDC curve. It can be seen that with the decrease of the submergence depth, from case A2H1K2 to case A2H3K2, the plants' deformation decreases in general. Although the influence of submergence on the deformation magnitude is less significant compared with the plant stiffness ratio and spacing, the flatness of the PDC curve for the cross-flow deformation and the projection height is apparent. The distribution density of the secondary peak increases statistically relative to the main one with η decreases. This can be interpreted by the upper layer flow structures. For the cases with large submergence depth, large vortex structures, including the K-H vortex, may dominate the deformation of the plants. Under the conditions, a large group of plants may be subjected to the same vortex actions and therefore exhibit similar deformations, which leads to a high peak on the PDC curve. However, for the cases with small submergence depth, there is no such vortexes exist and the plants' dynamics

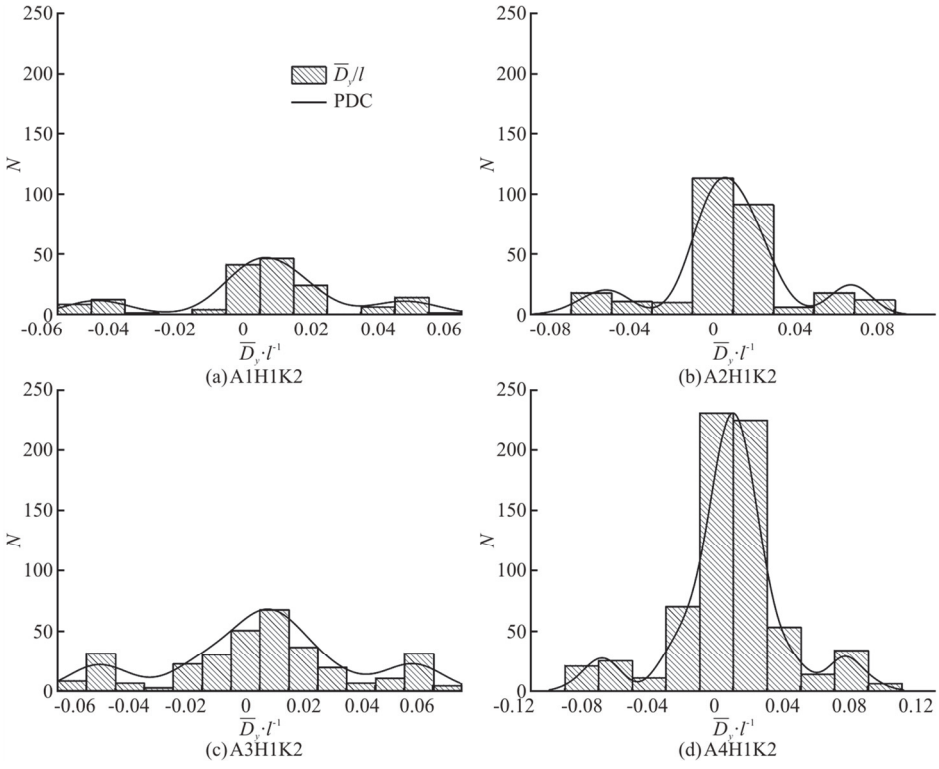

Fig. 11 Histogram of the probability distribution for cross-flow deformation of plants with various spacings

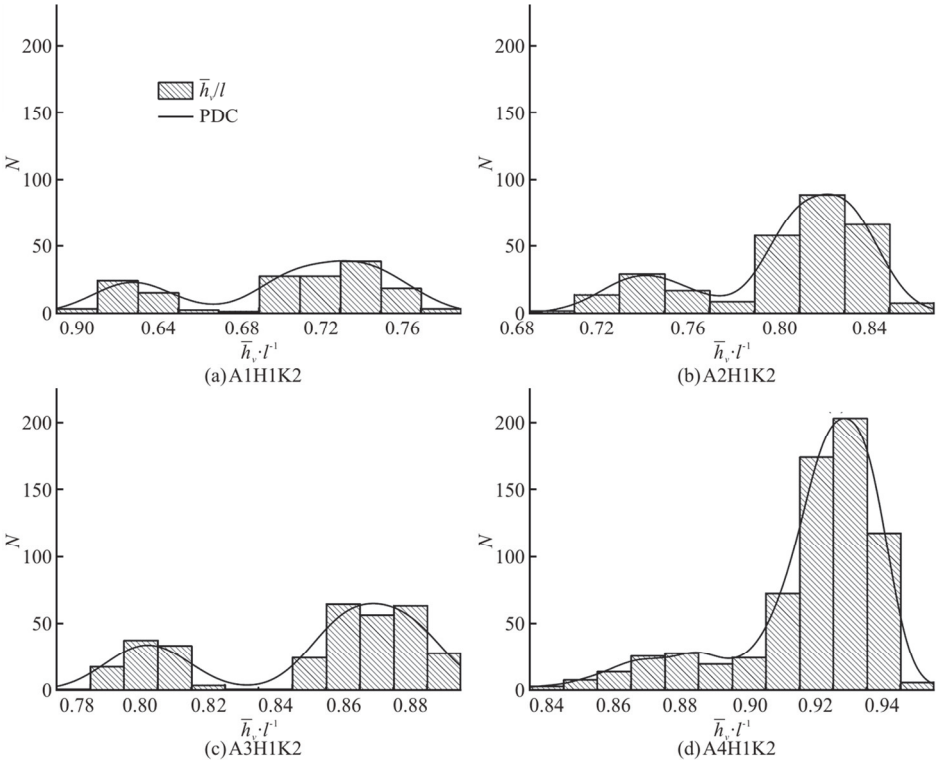

Fig. 12 Histogram of the probability distribution for projection height of plants with various spacings

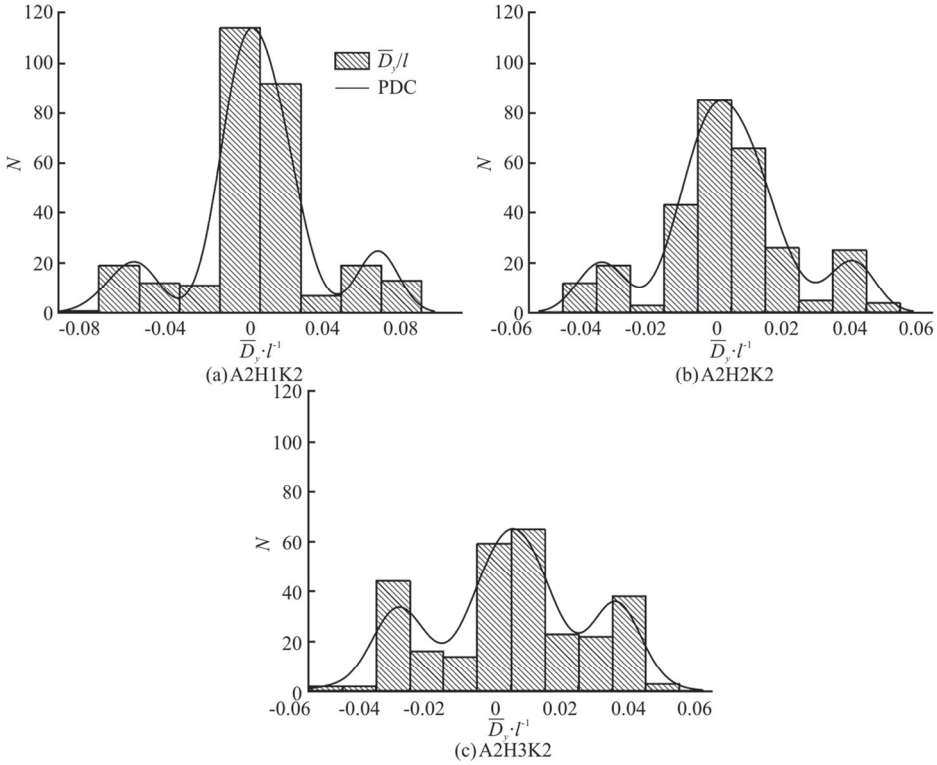

Fig. 13 Histogram of the probability distribution for cross-flow deformation of plants with various submergence

are mainly subjected to smaller flow structures relatively uniformly distributed in the channel.

3.2 *Fluid induced vegetation dynamics*

Under the action of the fluid forces, flexible

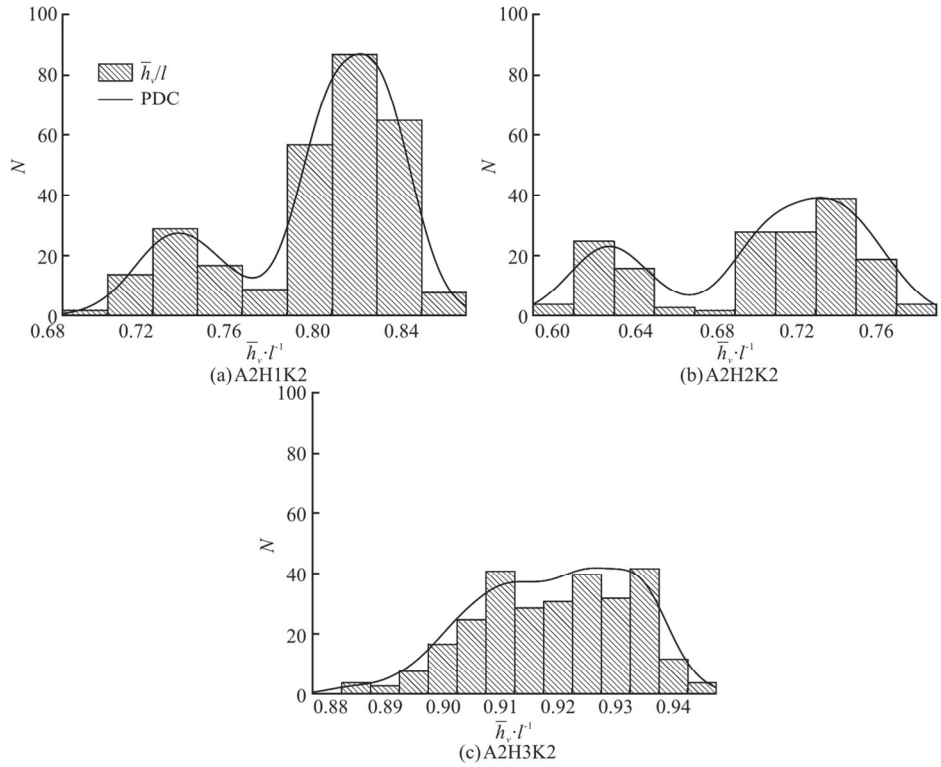

Fig. 14 Histogram of the probability distribution for projection height of plants with various submergence

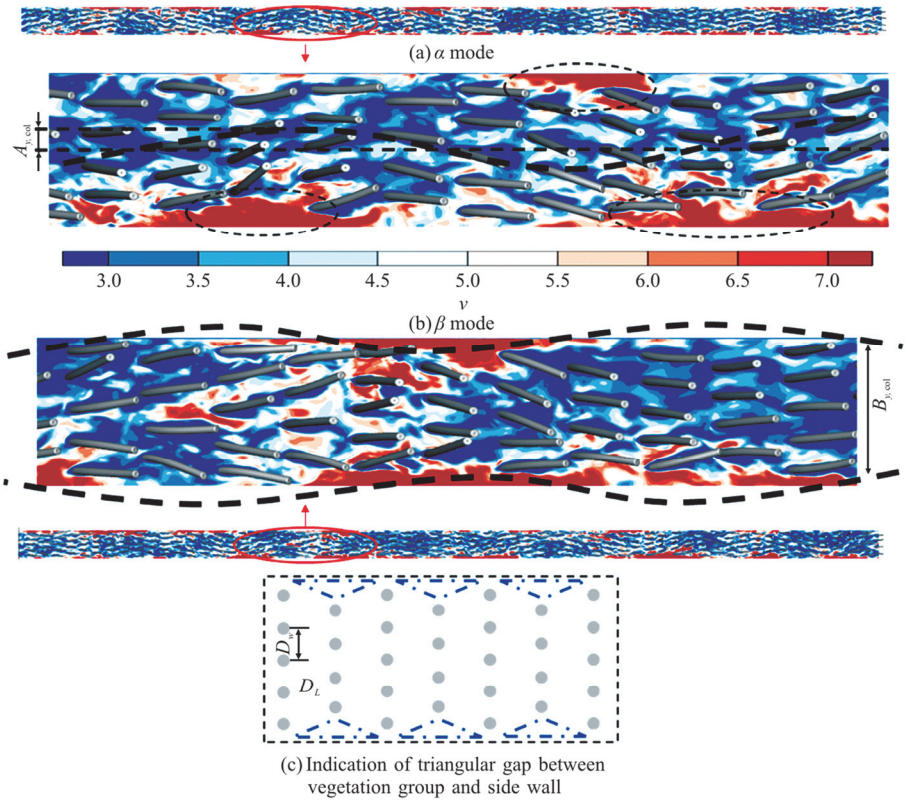

Fig. 15 (Color online) Instantaneous distribution of plant posture and flow velocity (case A2H1K2)

vegetations not only exhibit deformation in the streamwise and transverse direction, but also swing and oscillates dynamics with time, namely at a status of fluid-induced vibrations (FIVs). The FIVs of a single-cylinder itself involves quite complex fluid-structural interaction mechanisms, including vortex-induced vibration, galloping and lock-in regimes, and so on. Besides such cylinder-scale vibrations, uniformly distributed multiple vegetations demonstrate complex channel-scale waving motions as well, see Fig. 15.

Two different modes of waving motions are observed in the simulations, namely the α mode, the β mode. Here, the α mode is defined as the plants swinging back and forth in the transverse direction, which looks similar to the meandering flow in curved river channels, see Fig. 15(a), while the β mode means that the plants alternately gather toward the mid-plane and diverge to the sides, which looks like the pulsive contraction wave along artery blood vessel of human being, see Fig. 15(b). The substantial mechanism driving such waving patterns is inferred to need further investigations. According to our current observations, due to the staggered arrangement of the plants, there are large triangular gaps between the sidewall and the adjacent three plants, as indicated by the blue dotted area in Fig. 15(c). u_{tri}^{+}, u_{tri}^{-} is the velocity within the triangle area in the $+Y$, $-Y$ direction at the same downstream position. The movement of vegetation groups in the cross-flow direction is closely related to the relative size between u_{tri}^{+}, u_{tri}^{-}. A noticeable difference in flow velocity on both sides ($u_{\mathrm{tri}}^{+} > u_{\mathrm{tri}}^{-}$ or $u_{\mathrm{tri}}^{+} < u_{\mathrm{tri}}^{-}$) causes the plants at the same downstream position to move to one side, as shown in Fig. 15(a). However, when the flow velocity values on both sides are similar ($u_{\mathrm{tri}}^{+} \approx u_{\mathrm{tri}}^{-}$), the plants will move closer to the middle if this velocity is large, else, they diverge to the two different sides. Therefore, the closer the plant is to the sidewall, the more affected it is by the triangular gap, the larger its deformation in both downstream and transverse directions, and the lower the corresponding projection height, resulting in the appearance of secondary peaks in histograms. In general, both the α mode, the β mode waving motions of the vegetations are linked with the downstream traveling large vortex structures in the open channel, which are generated by the interaction between flow shearing and flexible vegetation motions. The co-exists of the two modes also imply that such vortexes have 3-D structures rather than simple 2-D structures like the K-H vortex.

To describe the waving motion amplitude of the vegetation groups in both the α mode, the β mode, two characteristic parameters are defined: The instantaneous average deformation amplitude $\langle A_{v,\mathrm{col}} \rangle$ represents the amplitude of the α mode, and the average span in a moment $\langle B_{v,\mathrm{col}} \rangle$ is used to characterize the amplitude of β mode, see Figs.15(a), 15(b). The spatial and temporal histories of the waving amplitude are shown in Fig. 16. In the contour for the α mode, see Fig. 16(a), the red parts indicate $\langle A_{v,\mathrm{col}} \rangle > 0$, that is, a column of plants moving in the $+Y$ direction as a whole, while the blue parts are opposite. Nevertheless, for the β mode, the red in the contour represents $\langle B_{v,\mathrm{col}} \rangle > 0$, this indicates that the span of a column of plants increases in the transverse flow, that is, these plants diverge to both sides. By contrast, the blue parts in Fig. 16(b) show

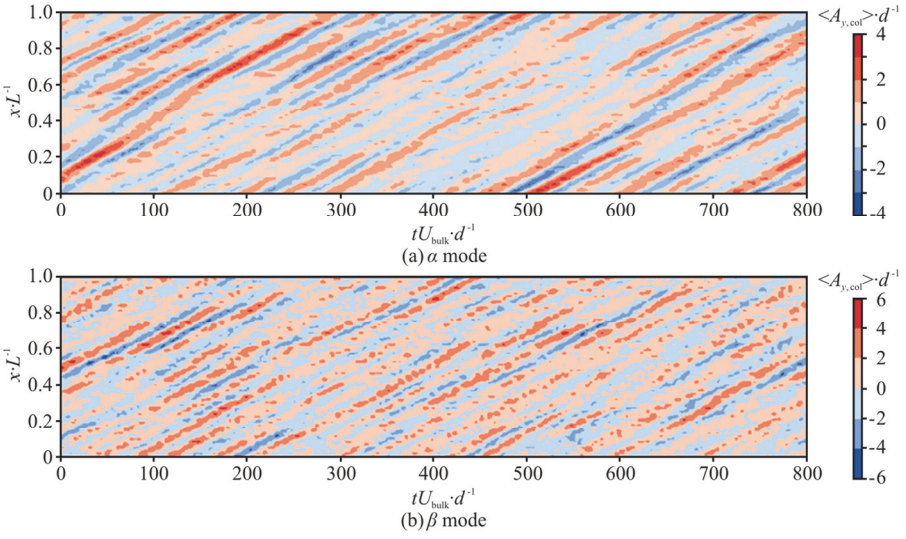

Fig. 16 (Color online) Spatiotemporal distribution of the plant deformation amplitude in cross-flow direction (A2H1K2)

these plants moving towards the center. Oblique stripes indicate that the α mode, β mode of the vegetation continuously spread downstream along the flow direction over time.

Spectral analyses are carried out to investigate the frequency feature of the waving motion of flexible vegetations, see Fig. 17. It can be seen that the primary and secondary frequencies of the α mode's amplitude $\left\langle A_{v,\mathrm{col}} \right\rangle$ are $f_{\alpha,1} = 0.270\ \mathrm{Hz}$, $f_{\alpha,2} = 0.320\ \mathrm{Hz}$, respectively. $f_{\alpha,2}$ is exactly equal to the dominant frequency of the amplitude under β mode, which shows that $\left\langle A_{v,\mathrm{col}} \right\rangle$ is affected by both α mode, β mode motion. This provides further evidence that the movement of plants in cross-flow is a superposition of the two periodic motions. In addition, there is a second frequency $f_{\beta,3} = 0.256\ \mathrm{Hz}$ in the frequency-space distribution of $\left\langle B_{v,\mathrm{col}} \right\rangle$, which is equal to the first-order natural frequency f_1^* of the plant. What's more, is also very close to f_1^*, meaning that α mode, β mode of vegetation movement in the cross-flow direction are closely related to the nature of the plant itself.

To further study the frequency distribution of $\left\langle B_{y,\mathrm{col}} \right\rangle$ and the occurrence of another sub-frequency $f_{\beta,2} = 0.384\ \mathrm{Hz}$, it is necessary to consider the movement of vegetation groups in other directions. In addition, the projection height of plants decreases significantly at the position it passes through due to the continuous downstream transmission of the K-H vortex, see Fig. 18. As a result, the projection height of vegetation at different downstream positions may also fluctuate to some extent. K-H vortex's intensity and traveling speed may change with time in the propagation process, so the amplitude of vegetation group fluctuation along the path will also change constantly. Such vortex-induced waving motions are usually named Monami phenomena, which are widely witnessed in field observations.

The relationship between the frequency of the K-H vortex f_{KH} and the plant's natural frequency f_1^* is the key to affecting vegetation's movement under the action of water flows[16]. The K-H vortexes in the present simulation share a frequency of $f_{\mathrm{KH}} \approx 0.097$ according to an estimation using Eq. (6). This frequency is much lower than the first-order natural frequency of the plant, which is $f_1^* = 0.256\ \mathrm{Hz}$. According to the results of Sundin and Bagheri[16], if $f_{\mathrm{KH}} < f_1^*$, the vegetation will immediately respond to the K-H vortex and interact with the turbulent flows, and finally reach equilibrium. To further analyze the movement rule of vegetation in the height direction, $\left\langle h_{v,\mathrm{col}} \right\rangle$ is defined as the instantaneous projection height mean value of the same column of vegetation referring $\left\langle h_{v,\mathrm{col}} \right\rangle$, $\left\langle B_{y,\mathrm{col}} \right\rangle$. The spatiotemporal distribution and frequency distribution of A2H1K2 are shown in Figs. 19, 20, respectively.

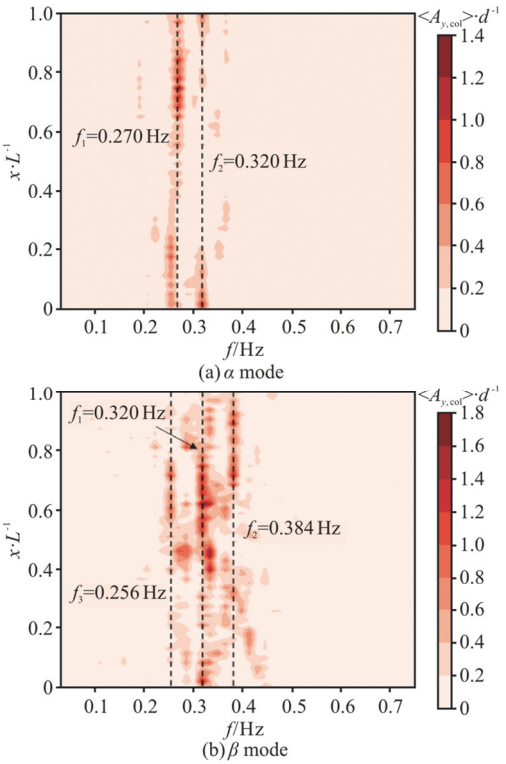

Fig. 17 (Color online) Frequency distribution of the plant deformation amplitude quadratic in cross-flow direction (A2H1K2)

$$f_{KH} = 0.032\left(\frac{\overline{u}}{\theta}\right) \tag{6}$$

It can be seen from the above figures that, the fluctuation of the projection height of plants also propagates downstream, but multiple frequencies dominate the change of $\left\langle h_{v,\mathrm{col}} \right\rangle$ at the same time. Still, the dominant frequency indicates that the movement of vegetation under β mode in a cross-flow direction is affected by the projection height. In addition, the first three frequencies marked by the black dotted line on the left in Fig. 20(b) are 0.097 Hz, 0.256 Hz and 0.320 Hz, which are consistent with f_{KH}, f_1^* and $f_{\beta,1}$, respectively. These consistencies imply that the fluctuation of the projected height of vegetation is

at least simultaneously affected by the K-H vortex, the nature of the plant itself, and the β mode of vegetation.

3.3 *Turbulent flow structures influenced by flexible vegetations*

The turbulent flow structures in vegetated open channels are influenced by the plants' time-averaged bending and the dynamic motion excited by flow vortexes of various scales. To clarify the influence of each factor, rigid vegetations with prescribed equivalent bending are adopted in the numerical simulations. Taking up-right vegetation (A2H1Rd) as an example, it can be seen from Fig. 21(a) that the flow velocity inside the vegetation is much lower than that in the free water layer due to the water-retardation effect from the vegetation. In addition, there is an obvious inflection point in the vertical profile of mean velocity near the top of vegetation ($z/l=1.0$) and a backward turn at the root of vegetation ($z/l\approx 0.08$), which may be caused by the horseshoe vortex[34]. This implies that the velocity does not monotone increase over depth as in well-known open channel velocity profiles, vegetated flows may demonstrate a thin layer of retarded flow with the lowest velocities in the middle.

When the equivalent stiffness ratio $K\geq 0.174$ (A2H1R6, A2H1R7), the vertical distribution of the average velocity is approximate to that of the up-right vegetation through the bending of the vegetation increases. But $\langle\overline{u}\rangle/U_{top}$ for vegetation at $K=0.087$

Fig. 18 (Color online) The instantaneous plant morphology and velocity distribution within the local area ($x/L=0.25$-0.75) of the vegetation (A2H1K2) (The positions of the same K-H vortex at different times are marked inside the red circle)

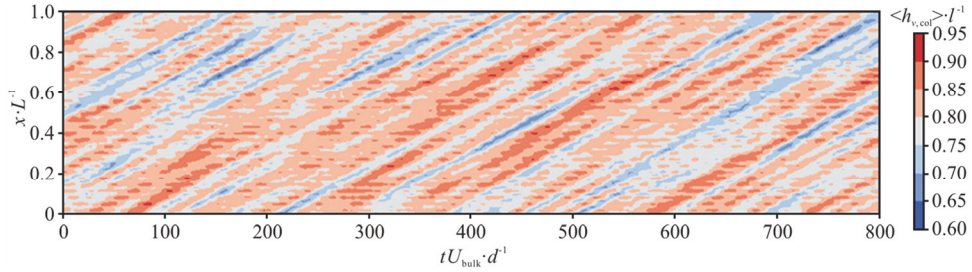

Fig. 19 (Color online) Spatiotemporal distribution of the vegetation's instantaneous projection height (A2H1K2)

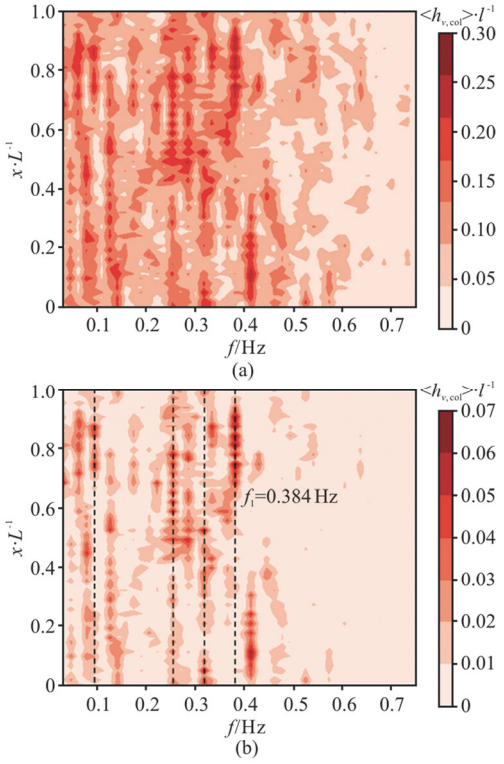

Fig. 20 (Color online) Frequency distribution of the vegetation's instantaneous projection height (A2H1K2)

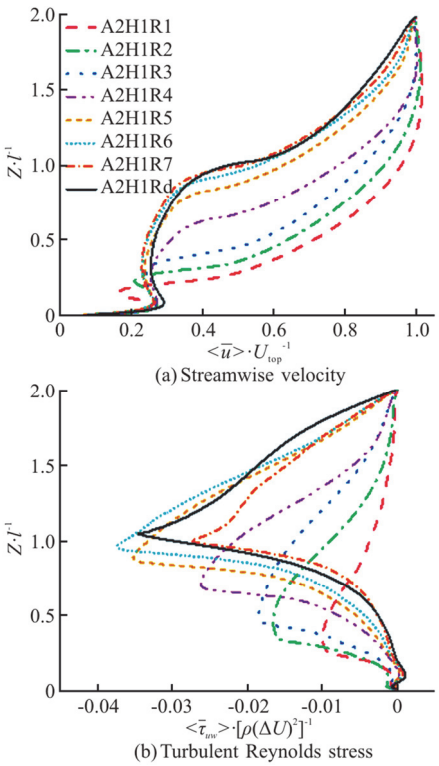

Fig. 21 (Color online) Vertical distribution of flow structures for rigid vegetation with different equivalent stiffness ratios

(A2H1R5) approximates that of up-right plants but increases in the free water layer. For A2H1R1-A2H1R4, it increases first, then decreases inside the vegetation and increases significantly in the free water layer with the lower equivalent stiffness ratio relative to the up-right vegetation. In addition, with the decrease of $\langle \overline{h}_v \rangle / l$, the backward turn position of the average velocity on the vertical distribution caused by the horseshoe vortex decreases slightly but remains at $0.05 \le z / l \le 0.07$.

The momentum exchange in the mixing layer can be characterized by the Reynolds stress $\tau_{uw} = \rho \overline{u'w'}$, which represent the fluctuating streamwise and vertical velocities, respectively. The time- and space-averaged non-dimensional Reynolds stress $\langle \overline{\tau}_{uw} \rangle / \rho(\Delta U)^2$ in different cases is shown in Fig. 21(b), and its absolute maximum value is listed in Table 5. It can be seen from Table 5 that $\left| \langle \overline{\tau}_{uw} \rangle / \rho(\Delta U)^2 \right|$ increases with the increase when $K \le 0.174$ or $\langle \overline{h}_v \rangle / l < 0.9$ (A2H1R1-A2H1R6). However, when $K \ge 0.174$ or $\langle \overline{h}_v \rangle / l > 0.9$, $\left| \langle \overline{\tau}_{uw} \rangle / \rho(\Delta U)^2 \right|$ remains between 0.28, 0.37. As the water depth increases (see Fig. 21(b)), $\left| \langle \overline{\tau}_{uw} \rangle / \rho(\Delta U)^2 \right|$ it increases rapidly within the vegetation but decreases above the plants. Therefore, the location of the transition can be used as a border to

Table 5 Turbulent characteristics of rigid vegetated flow with different equivalent stiffness ratios

Case	$\langle \overline{h}_v \rangle / l$	z_m / l	$\lvert \langle \overline{\tau}_{uw} \rangle / \rho(\Delta U)^2 \rvert$	δ_e / l	$\delta_e / \langle \overline{h}_v \rangle$
A2H1R1	0.173	0.359	0.010	0.046	0.268
A2H1R2	0.262	0.469	0.017	0.124	0.472
A2H1R3	0.364	0.516	0.018	0.178	0.488
A2H1R4	0.600	0.703	0.026	0.299	0.487
A2H1R5	0.792	0.891	0.035	0.388	0.490
A2H1R6	0.881	0.953	0.037	0.411	0.467
A2H1R7	0.944	1.000	0.028	0.434	0.460
A2H1Rd	1.000	1.047	0.034	0.463	0.463

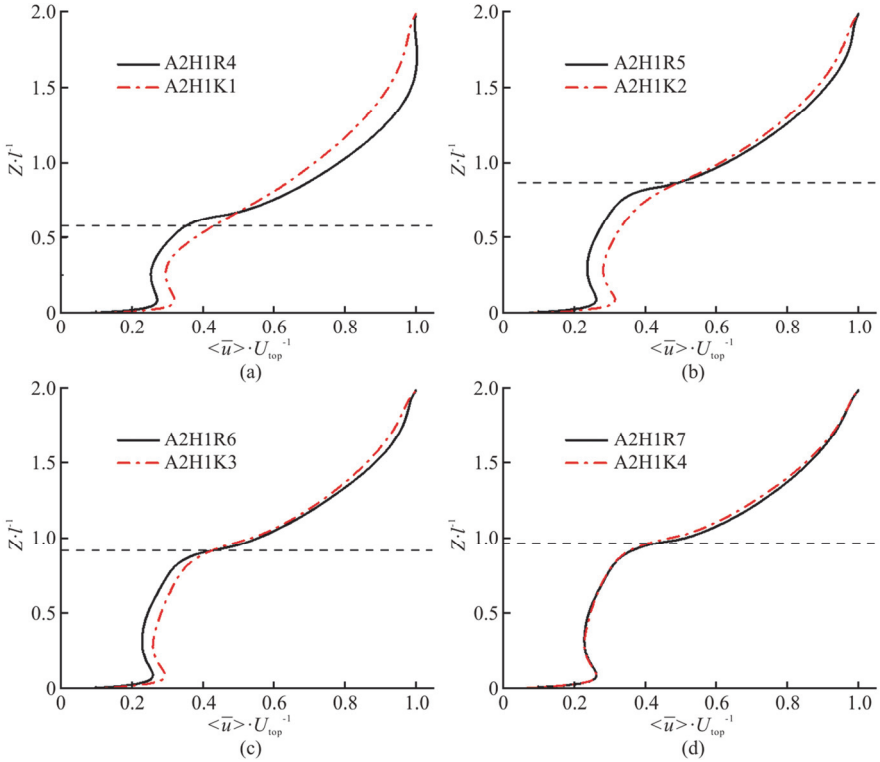

Fig. 22 (Color online) Vertical mean velocity flow profiles in channels with rigid and flexible vegetations (The two curves in each subplot shares the same bending, "R" refers to rigid, "K" refers to flexible case)

distinguish the vertical and horizontal exchange areas within the vegetation. Nepf and Vivoni[35] defined the penetration depth δ_e of the K-H vortex as the distance from the top of the vegetation to the border between vertical and horizontal exchange areas. The $\delta_e / \langle \overline{h}_v \rangle$ of vegetation remains between 0.46-0.49 except the case at $K = 0.001$ (A2H1R1).

The flexible vegetations are subjected to complex FIVs rather than a steady bending, which involves both streamwise and cross-flow motions, and the deformation in the streamwise even reaches 36.55 times that in the cross-flow direction at case A1H1K2. The deformation of plants is intensified as the stiffness increases but slightly when the spacing or submergence gets greater. The higher the vegetations, the larger the turbulent Reynolds stress of the open-channel flow, which remains between 0.01, 0.37.

The dimensionless average velocity $\langle \overline{u} \rangle / U_{\text{top}}$ of rigid vegetation with equivalent bending significantly decreases within the vegetation but increases in the free water layer when the stiffness ratio of the plant meets $K \le 0.044$ at the same average projection height (see Fig. 22, U_{top} is the velocity at the top of vegetation). The velocity gradient at the inflection point with flexible vegetation is smaller than that of the rigid case. This may be due to the movement range of flexible vegetation being large with a small stiffness ratio K, and the water structure

of the free water layer intrudes into the vegetation with the development of the K-H vortex so that the free water near the top of vegetation is fully mixed with water inside the vegetation, which is why this area is called the mixing layer. While if $0.087 \le K \le 0.174$, the $\langle \overline{u} \rangle / U_{\text{top}}$ within the rigid vegetation is significantly larger than that of the flexible vegetation but consistent in the free water layer. Therefore the motion amplitude of flexible vegetation decreases with the increase of K, reducing the influence of vegetation motion on the free water layer. As K continues to increase $(K \ge 0.347)$, the motion amplitude of flexible vegetation decreases further and the $\langle \overline{u} \rangle / U_{\text{top}}$ approximately equal with the two vegetations throughout the water.

The Reynolds stress, $\langle \overline{\tau}_{uw} \rangle / \rho(\Delta U)^2$ of turbulent flows in open channels with flexible plants are presented in Fig. 23, Table 6. It can be seen that when the projection height is within $0.60 < \langle \overline{h}_v \rangle / l < 0.95$, the dimensionless Reynolds stress and the intrusion depth of the K-H vortex are around $\langle \overline{\tau}_{uw} \rangle / \rho(\Delta U)^2 = 0.052 - 0.067$, $\delta_e / \langle \overline{h}_v \rangle = 0.60 - 0.75$ respectively, which increases by 70%-100%, 30%-50% compared with the simulation results of rigid vegetation under the same bending amplitude, which are $\langle \overline{\tau}_{uw} \rangle / \rho(\Delta U)^2 = 0.026 - 0.037$, $\delta_e / \langle \overline{h}_v \rangle = 0.46 - 0.49$, respectively. The movement of multiple flexible plants significantly enhance the mixing in both the free water layer and the vegetation layer. The Reynolds stress, $\langle \overline{\tau}_{uw} \rangle / \rho(\Delta U)^2$ decreases by around 50% when the spacing of flexible vegetation increases by four times but increases by around 400% when the submergence decreases by 40%. Therefore the change of submergence has a more significant impact on the mixing layer than the spacing. The K-H vortex intrusion depth, $\delta_e / \langle \overline{h}_v \rangle$ decreases in general as the spacing of vegetation increases, which may be interpreted by the increased shielding effect of vegetation on its interior when vegetation density rises.

In summary, the wave motion of flexible vegetation in open-channel flow exhibits α mode, β mode, which affects the fluctuation of vegetation with the K-H vortex and the nature of the plant itself. Moreover, the instantaneous average deformation amplitude of α mode is about four times larger than that of β mode. Compared with the rigid bent-shaped plants under the same bending amplitude, the behaviors of flexible vegetation may increase turbulent Reynolds stress of the open-channel flow by 70%-100% and increase the K-H vortex invasion depth by 30%-50%.

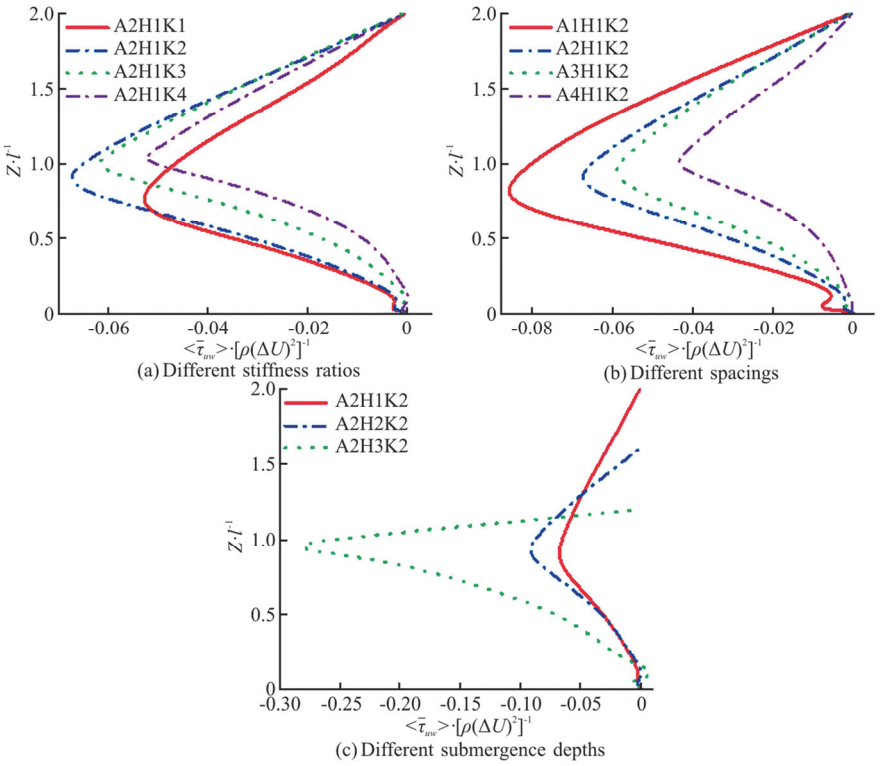

Fig. 23 (Color online) Vertical Reynolds stress profiles in channels with flexible vegetations

Table 6 Turbulent characteristics of flexible plants under different working cases

Case	$\langle \overline{h}_v \rangle / l$	z_m / l	$\lvert \langle \overline{\tau}_{uw} \rangle / \rho(\Delta U)^2 \rvert$	δ_e / l	$\delta_e / \langle \overline{h}_v \rangle$
A2H1K1	0.613	0.766	0.053	0.449	0.732
A2H1K2	0.803	0.906	0.067	0.597	0.746
A2H1K3	0.921	1.000	0.062	0.629	0.683
A2H1K4	0.973	1.031	0.052	0.577	0.593
A1H1K2	0.698	0.812	0.086	0.515	0.739
A2H1K2	0.803	0.906	0.067	0.597	0.746
A3H1K2	0.842	0.953	0.059	0.617	0.733
A4H1K2	0.903	1.016	0.043	0.573	0.635
A2H1K2	0.803	0.906	0.067	0.597	0.746
A2H2K2	0.858	0.938	0.091	0.537	0.626
A2H3K2	0.915	0.956	0.281	0.634	0.693

4. Conclusions

To explore the dynamics of submerged flexible vegetations in turbulent open-channel flows and its feedback to turbulent flow structures, numerical simulations are carried out using a fluid-structure interaction solver, which couples the LES model for turbulent flow and the VFIFE method for flexible solid via IB technique. Up to 720 shape-resolved vegetations with different flexibility, spacing, and submergence are simulated. Based on the numerical simulation results, the main conclusions are as follows:

(1) The flexible vegetations are subjected to complex FIVs rather than a steady bending. The FIV involves both streamwise and cross-flow motions driven by both small-scale shedding vortex and large-scale K-H vortex in the canopy layer. Under the lateral restrain of channel side walls, such K-H vortexes exhibit obvious 3-D features. The streamwise deformation is always stronger than that of transverse direction, and their ratio is even up to 36.55.

(2) In relatively long and narrow open channels, the vegetation group exhibits interesting pulsive wave motions of different patterns, namely the α, β modes. α mode is the serpentine wave motion of the vegetation in the cross-flow direction, which is caused by the high-velocity area at the gaps on both sides of the wall. While β mode is the periodic gathering-diverging behaviors of vegetation. In addition, the motion of the vegetation is a superposition of α mode, β mode, and the K-H vortex-induced fluctuation. Moreover, the instantaneous average deformation amplitude of α mode is about four times larger than that of β mode.

(3) Compared with the rigid bent-shaped plants under the same bending amplitude, the dynamics of flexible vegetation may increase turbulent Reynolds stress of the open-channel flow by 70%-100% and increase K-H vortex invasion depth by 30%-50%, which implies that the FIV of vegetations leads to higher flow energy dissipation and stronger turbulent mixing.

(4) The Reynolds stress of the turbulent flow in the open channel with flexible vegetations decreases by around 50% when the spacing of adjacent plant increases by four times. It increases by around 400% when the submergence decreases by 40% from 2 to 1.2 times of the plant height. Reynolds stress is found to be more sensitive to the submergence depth than the distribution density according to present simulations.

Acknowledgment

This work was supported by the Open Fund of State Key Laboratory of Hydraulics and Mountain River Engineering, Sichuan University.

References

[1] Peralta G., Brun F. G., Perez-Llorens J. L. et al. Direct effects of current velocity on the growth, morphometry and architecture of seagrasses: A case study on Zostera noltii [J]. *Marine Ecology Progress*, 2006, 327: 135-142.

[2] Huai W. X., Li S., Katul G. G. et al. Flow dynamics and sediment transport in vegetated rivers: A review [J]. *Journal of Hydrodynamics*, 2021, 33(3): 400-420.

[3] Williamson C. H. K., Roshko A. Vortex formation in the wake of an oscillating cylinder [J]. *Journal of Fluids and Structures*, 1988, 2(4): 355-381.

[4] Nepf H., Ghisalberti M. Flow and transport in channels with submerged vegetation [J]. *Acta Geophysica*, 2008, 56(3): 753-777.

[5] Nezu I., Sanjou M. Turburence structure and coherent motion in vegetated canopy open-channel flows [J].

Journal of Hydro-environment Research, 2008, 2(2): 62-90.

[6] Nikora N., Nikora V., O'Donoghue T. Velocity profiles in vegetated open-channel flows: Combined effects of multiple mechanisms [J]. *Journal of Hydraulic Engineering, ASCE*, 2013, 139(10): 1021-1032.

[7] Denny M. W., Gaylord B. P., Cowen E. A. Flow and flexibility. II. The roles of size and shape in determining wave forces on the bull kelp nereocystis luetkeana [J]. *Journal of Experimental Biology*, 1997, 200(24): 3165-3183.

[8] Fonseca M. S., Koehl M. A. R., Kopp B. S. Biomechanical factors contributing to self-organization in seagrass landscapes [J]. *Journal of Experimental Marine Biology and Ecology*, 2007, 340(2): 227-246.

[9] Bradley K., Houser C. Relative velocity of seagrass blades: Implications for wave attenuation in low-energy environments [J]. *Journal of Geophysical Research: Earth Surface*, 2009, 114(F1): F01004.

[10] Ghisalberti M., Nepf H. M. Mixing layers and coherent structures in vegetated aquatic flows [J]. *Journal of Geophysical Research-Oceans*, 2002, 107(C2): 3011.

[11] Luhar M., Nepf H. M. Flow-induced reconfiguration of buoyant and flexible aquatic vegetation [J]. *Limnology and Oceanography*, 2011, 56(6): 2003-2017.

[12] Chen H., Zou Q. P. Eulerian–Lagrangian flow-vegetation interaction model using immersed boundary method and OpenFOAM [J]. *Advances in Water Resources*, 2019, 126: 176-192.

[13] Huai W., Zhang J., Katul G. G. et al. The structure of turbulent flow through submerged flexible vegetation[J]. *Journal of Hydrodynamics*, 2019, 31(2): 274-292.

[14] Silva-Leon J., Cioncolini A. Experiments on flexible filaments in air flow for aeroelasticity and fluid-structure interaction models validation [J]. *Fluids*, 2020, 5(2): 90.

[15] O'Connor J., Revell A. Dynamic interactions of multiple wall-mounted flexible flaps [J]. *Journal of Fluid Mechanics*, 2019, 870: 189-216.

[16] Sundin J., Bagheri S. Interaction between hairy surfaces and turbulence for different surface time scales [J]. *Journal of Fluid Mechanics*, 2019, 861: 556-584.

[17] Zhang X., He G., Zhang X. Fluid–structure interactions of single and dual wall-mounted 2D flexible filaments in a laminar boundary layer [J]. *Journal of Fluids and Structures*, 2020, 92: 102787.

[18] Lee T., Lin C. L., Friehe C. A. Large-eddy simulation of air flow around a wall-mounted circular cylinder and a tripod tower [J]. *Journal of Turbulence*, 2007, 8: N29.

[19] Palau-Salvador G., Stoesser T., Froehlich J. et al. Large eddy simulations and experiments of flow around finite-height cylinders [J]. *Flow Turbulence and Combustion*, 2010, 84(2): 239-275.

[20] Long X., Cheng H., Ji B. et al. Large eddy simulation and Euler-Lagrangian coupling investigation of the transient cavitating turbulent flow around a twisted hydrofoil [J]. *International Journal of Multiphase Flow*, 2018, 100: 41-56.

[21] Cheng H. Y., Bai X. R., Long X. P. et al. Large eddy simulation of the tip-leakage cavitating flow with an insight on how cavitation influences vorticity and turbulence [J]. *Applied Mathematical Modelling*, 2020, 77: 788-809.

[22] Huai W., Xue W., Qian Z. Large-eddy simulation of turbulent rectangular open-channel flow with an emergent rigid vegetation patch [J]. *Advances in Water Resources*, 2015, 80: 30-42.

[23] Gong Y., Stoesser T., Mao J. et al. LES of flow through and around a finite patch of thin plates [J]. *Water Resources Research*, 2019, 55(9): 7587-7605.

[24] Liu M., Huai W., Ji B. Characteristics of the flow structures through and around a submerged canopy patch [J]. *Physics of Fluids*, 2021, 33(3): 035144.

[25] Smagorinsky J. General circulation experiments with the primitive equations [J]. *Monthly Weather Review*, 1963, 91: 99-164.

[26] Shih C., Wang Y. K., Ting E. C. Fundamentals of a vector form intrinsic finite element: Part III. Convected material frame and examples [J]. *Journal of Mechanics*, 2004, 20(2): 133-143.

[27] Ting E. C., Shih C., Wang Y. K. Fundamentals of a vector form intrinsic finite element: Part I. Basic procedure and a plane frame element [J]. *Journal of Mechanics*, 2004, 20(2): 113-122.

[28] Ting E. C., Shih C., Wang Y. K. Fundamentals of a vector form intrinsic finite element: Part II. Plane solid elements [J]. *Journal of Mechanics*, 2004, 20(2): 123-132.

[29] Uhlmann M. An immersed boundary method with direct forcing for the simulation of particulate flows [J]. *Journal of Computational Physics*, 2005, 209(2): 448-476.

[30] Ji C., Munjiza A., Williams J. J. R. A novel iterative direct-forcing immersed boundary method and its finite volume applications [J]. *Journal of Computational Physics*, 2012, 231(4): 1797-1821.

[31] Chen W., Ji C., Alam M. M. et al. Numerical simulations of flow past three circular cylinders in equilateral-triangular arrangements [J]. *Journal of Fluid Mechanics*, 2020, 891: A14.

[32] Chen W., Ji C., Alam M. M. et al. Flow-induced vibrations of a D-section prism at a low Reynolds number [J]. *Journal of Fluid Mechanics*, 2022, 941: A52.

[33] Etminan V., Lowe R. J., Ghisalberti M. A new model for predicting the drag exerted by vegetation canopies [J]. *Water Resources Research*, 2017, 53: 3179-3196.

[34] Liu D., Diplas P., Fairbanks J. D. et al. An experimental study of flow through rigid vegetation [J]. *Journal of Geophysical Research: Earth Surface*, 2008, 113(4): F04015.

[35] Nepf H. M., Vivoni E. R. Flow structure in depth-limited, vegetated flow [J]. *Journal of Geophysical Research: Oceans*, 2000, 105(C12): 28547-28557.